

A new class of high-entropy M_3B_4 borides

Mingde QIN, Qizhang YAN, Yi LIU, Jian LUO*

Department of NanoEngineering, Program of Materials Science and Engineering,
University of California, San Diego, La Jolla, CA, 92093, USA

Received: September 18, 2020; Revised: October 29, 2020; Accepted: November 9, 2020

© The Author(s) 2020.

Abstract: A new class of high-entropy M_3B_4 borides of the Ta_3B_4 -prototyped orthorhombic structure has been synthesized in the bulk form for the first time. Specimens with compositions of $(V_{0.2}Cr_{0.2}Nb_{0.2}Mo_{0.2}Ta_{0.2})_3B_4$ and $(V_{0.2}Cr_{0.2}Nb_{0.2}Ta_{0.2}W_{0.2})_3B_4$ were fabricated via reactive spark plasma sintering of high-energy-ball-milled elemental boron and metal precursors. The sintered specimens were ~98.7% in relative densities with virtually no oxide contamination, albeit the presence of minor (4–5 vol%) secondary high-entropy M_5B_6 phases. Despite that Mo_3B_4 or W_3B_4 are not stable phase, 20% of Mo_3B_4 and W_3B_4 can be stabilized into the high-entropy M_3B_4 borides. Vickers hardness was measured to be 18.6 and 19.8 GPa at a standard load of 9.8 N. This work has further expanded the family of different structures of high-entropy ceramics reported to date.

Keywords: high-entropy ceramics; high-entropy borides; reactive sintering; spark plasma sintering; Ta_3B_4 -prototyped orthorhombic structure

1 Introduction

In 2004, Yeh *et al.* [1] and Cantor *et al.* [2] independently reported the fabrication of high-entropy alloys (HEAs), which has stimulated significant research interests. HEAs, which are more broadly defined as “complex-concentrated or compositionally-complex alloys (CCAs)”, have shown excellent, often unexpected, mechanical and physical properties [3]. In last five years, high-entropy ceramics (HECs), including high-entropy oxides [4–7], borides [8–10], carbides [11–13], silicides [14, 15], and fluorides [16], have been synthesized in the bulk form as the ceramic counterparts to HEAs. Recently, it was proposed to generalize HECs to “compositionally-complex ceramics (CCCs)”, where medium-entropy and/or non-equimolar compositions can outperform

their high-entropy counterparts [17,18].

In 2016, Gild *et al.* [8] first reported the synthesis of single-phase high-entropy diborides in AlB_2 -prototyped hexagonal structure, which represents the first high-entropy boride (HEB) fabricated. Follow-up studies synthesized the high-entropy diborides from boro/carbothermal reduction of metal oxides [19–21] or elemental precursors [22–24]. Only a limited number of studies explored the HEBs with other metal-to-boron stoichiometric ratios in monoboride (MB) or hexaboride (MB_6) structures [9,10,25]. Specifically, Qin *et al.* [9] fabricated a class of high-entropy monoborides, including $(V_{0.2}Cr_{0.2}Nb_{0.2}Ta_{0.2}W_{0.2})B$, $(V_{0.2}Cr_{0.2}Nb_{0.2}Mo_{0.2}Ta_{0.2})B$, and $(V_{0.2}Cr_{0.2}Nb_{0.2}Mo_{0.2}W_{0.2})B$, via a synthesis route of reactive spark plasma sintering (SPS) of elemental boron and metals. This flexible direct boron-metal reactive SPS method enables us to further explore HEBs of other metal-to-boron stoichiometric ratios.

* Corresponding author.
E-mail: jluo@alum.mit.edu

Ta₃B₄-prototyped M₃B₄ (M represents a transition metal) orthorhombic structure (space group: *Immm*, No. 71) is composed by stackings of metal cation bilayers and boron chain bilayers with metal cation monolayers in between. Figure 1 schematically illustrates a high-entropy M₃B₄ structure. Ti, V, Cr, Mn, Nb, and Ta are known to possess this M₃B₄ structure [26], and the M₃B₄ phases can be made from elemental precursors [27]. These binary M₃B₄ materials are known to possess both high melting point [27] and high hardness [26], and they are predicted to have good thermodynamic stability and elastic property [28]. To further explore the high-entropy materials of this structure, here, we applied the direct boron-metal *in-situ* reactive SPS method to synthesize (V_{0.2}Cr_{0.2}Nb_{0.2}Mo_{0.2}Ta_{0.2})₃B₄ and (V_{0.2}Cr_{0.2}Nb_{0.2}Ta_{0.2}W_{0.2})₃B₄ as high-entropy M₃B₄ borides for the first time, thereby expanding the family of HEBs specifically, and HECs in general.

2 Experimental

High-entropy M₃B₄ specimens were synthesized via *in-situ* reactive SPS based on the following nominal reactions: 0.6V + 0.6Cr + 0.6Nb + 0.6Mo + 0.6Ta + 4B → (V_{0.2}Cr_{0.2}Nb_{0.2}Mo_{0.2}Ta_{0.2})₃B₄, and 0.6V + 0.6Cr + 0.6Nb + 0.6Ta + 0.6W + 4B → (V_{0.2}Cr_{0.2}Nb_{0.2}Ta_{0.2}W_{0.2})₃B₄. Commercial elemental powders of V, Cr, Nb, Mo, Ta, and W (> 99.5% purity, ~325 mesh, purchased from Alfa Aesar, MA, USA) and boron (amorphous, 99% purity, 1–2 μm, purchased from US Research Nanomaterials,

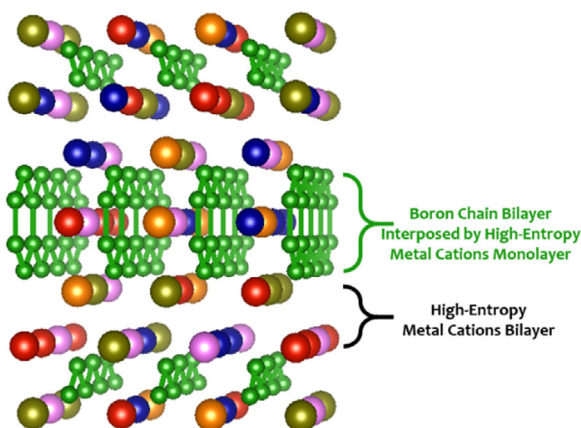


Fig. 1 Schematic illustration of the atomic structure of the Ta₃B₄-prototyped orthorhombic high-entropy M₃B₄ boride (space group: *Immm*, No. 71). This high-entropy structure is composed by stackings of high-entropy metal cations bilayer and boron chain bilayer (which is interposed by a high-entropy metal cations monolayer).

TX, USA) were utilized as precursors for making specimens listed in Table 1. For each composition, appropriate amounts of metals and boron powders were weighted out in batches of 5 g; 4 at% of excess boron was added (i.e., to keep a metal-to-boron atomic ratio of 3:4.16) to offset the boron loss due to reaction with native oxide and subsequent evaporation. The powders were first mixed by a vortex mixer, and successively high energy ball milled (HEBM) in a Spex 8000D mill (SpexCertPrep, NJ, USA) in tungsten carbide lined stainless steel jars and 11.2 mm tungsten carbide milling media (with a ball-to-powder ratio ≈ 4.5:1) for 50 min with 1 wt% (0.05 g) of stearic acid as a lubricant. After HEBM, as-milled powder mixtures were loaded into 10 mm graphite dies lined with graphite foils in batches of 2.5 g, and subsequently consolidated into dense pellets via SPS in vacuum (10⁻² Torr) using a Thermal Technologies 3000 series SPS (CA, USA). The HEBM, as well as the loading and handling of as-milled powder mixtures, were conducted in an argon atmosphere (with < 10 ppm O₂) to minimize oxidation. During SPS, specimens were first held isothermally at 1400 °C, and consecutively at 1600 °C, based on the procedure reported in a prior publication [24]; subsequently, the temperature was raised to 1900 °C at a heating rate of 30 °C/min, and maintained isothermally for 10 min, when the applied pressure was increased from 10 to 50 MPa at a rate of 5 MPa/min, for final densification. The *in-situ* reactions between metals and boron likely took place during the initial temperature ramping. After sintering, the specimens were cooled down to room temperature in a natural manner inside the SPS machine (with power off).

The sintered specimens were first ground to remove the carbon-contaminated surface layer from the graphite tooling, and polished before further characterizations. X-ray diffraction (XRD) characterizations were conducted on a Rigaku Miniflex diffractometer with Cu K α radiation at 30 kV and 15 mA. Densities were measured by the Archimedes method. Theoretical densities were calculated from the nominal stoichiometry and lattice parameters measured by XRD. Scanning electron microscopy (SEM), energy dispersive X-ray spectroscopy (EDS), and electron backscatter diffraction (EBSD) were conducted using a Thermo-Fisher (formerly FEI) Apreo microscope equipped with an Oxford N-Max^N EDX detector and an Oxford Symmetry EBSD detector. Vickers microhardness tests were carried out on a LECO diamond microindenter with a standard loading force

Table 1 Summary of the two high-entropy M_3B_4 borides studied. The theoretical densities are calculated from the measured lattice parameters and nominal compositions. Specimen densities are measured via the Archimedes method. Averaged grain sizes are obtained from electron backscatter diffraction (EBSD) analyses

Nominal composition	Measured lattice parameters by XRD, a, b, c (Å)	Theoretical density (g/cm^3)	Measured density (g/cm^3)	Relative density (%)	Grain size (μm)	Vickers hardness at 9.8 N (GPa)	Porosity by SEM (%)	Porosity + secondary phase by EBSD (%)	Secondary phase fraction (vol%)
$(V_{0.2}Cr_{0.2}Nb_{0.2}Mo_{0.2}Ta_{0.2})_3B_4$	3.183, 13.593, 3.060	8.20	8.09	98.7	12.2 ± 10.1	18.6 ± 1.2	~1.3	~5.3	~4.0
$(V_{0.2}Cr_{0.2}Nb_{0.2}Ta_{0.2}W_{0.2})_3B_4$	3.185, 13.574, 3.058	9.54	9.42	98.7	12.1 ± 10.3	19.8 ± 0.9	~1.5	~6.7	~5.2

of 9.8 N (1 kgf) with a holding time of 15 s, abiding by the ASTM Standard C1327. More than 30 measurements were conducted at different locations for each specimen to ensure the statistical validity and minimize the microstructural and grain boundary effects.

3 Results and discussion

Figure 2 shows the ram displacement for a typical sintering of high-entropy M_3B_4 specimen during the initial temperature ramping to 1400 °C, which can be further separated into three stages: (I) An initial heating stage to ~550 °C, with no significant ram displacement; (II) an *in-situ* metal-boron reaction stage at ~600 °C, where significant ram displacement is observed due to the exothermal self-propagating metal-boron reaction; and (III) a post-reaction stage, where the linear ram displacement is mainly due to the thermal expansion of specimen and graphite tooling. It can be clearly evident that the *in-situ* reaction between metal and boron powders (to form high-entropy M_3B_4)

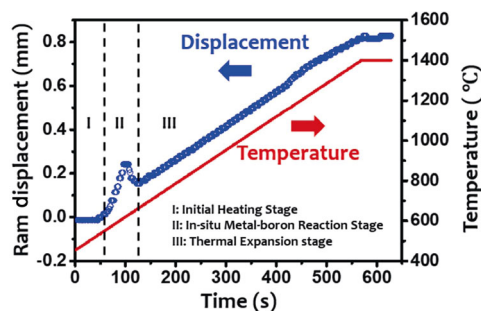


Fig. 2 SPS ram displacement for sintering of a typical high-entropy M_3B_4 specimen during the initial temperature ramping to 1400 °C. It is evident that the *in-situ* reaction between metal and boron powders (to form high-entropy M_3B_4) occurs during the temperature ramping at approx. 550–650 °C in the stage II labeled in Fig. 2.

occurs during the temperature ramping at approx. 550–650 °C.

XRD patterns of the as-milled powder mixtures (after HEBM, but before SPS) show multiple distinct BCC phases for both specimens (Fig. 3). Peak broadening observed in the milled powders can be attributed to the grain size reduction, lattice distortion, and micro-strains

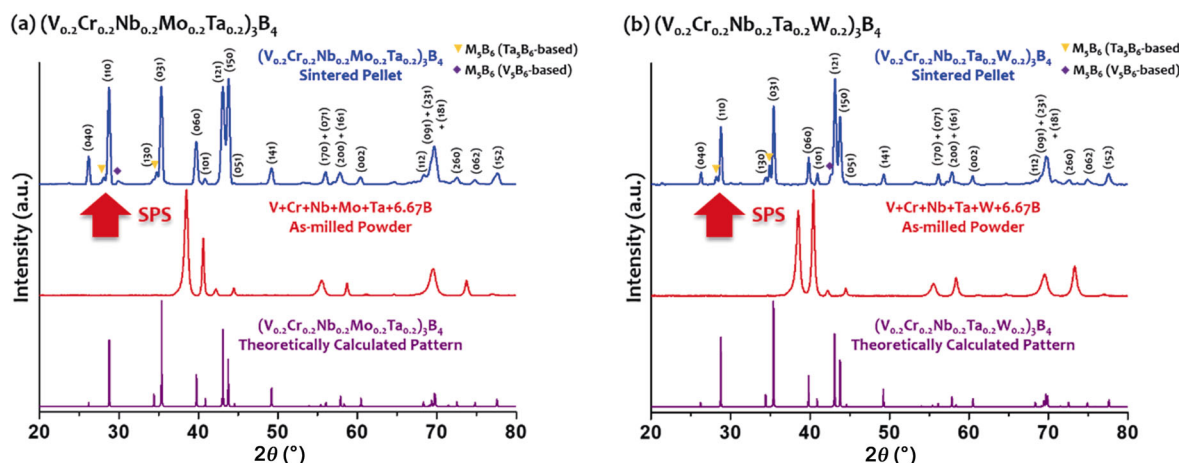


Fig. 3 XRD patterns of (a) $(V_{0.2}Cr_{0.2}Nb_{0.2}Mo_{0.2}Ta_{0.2})_3B_4$ and (b) $(V_{0.2}Cr_{0.2}Nb_{0.2}Ta_{0.2}W_{0.2})_3B_4$ specimens. For each composition, measured patterns of sintered pellets (after SPS) and as-milled powders mixtures (after HEBM), as well as calculated patterns for the ideal high-entropy M_3B_4 borides, are shown. Both sintered specimens show a major Ta_3B_4 -structured orthorhombic phase, with a minor amount of M_3B_6 secondary phases. Note that some diffraction peaks in the Ta_3B_4 -orthorhombic phase are overlapped, and the XRD patterns of as-milled powders are not indexed due to extensive peak overlapping of five metal elements.

developed during the HEBM. XRD shows that both sintered specimens primarily possess a Ta₃B₄-prototyped orthorhombic phase (Fig. 2). Minor amounts of M₃B₆ secondary phases, which likely include both the Ta₃B₆ [29] and V₃B₆ [30] based phases (space group: *Cmmm*, or equivalently *Ammm*, No. 65), were also observed in sintered specimens. The calculated XRD patterns based on the nominal compositions and measured lattice parameters from XRD on sintered specimens (listed in Table 1), assuming random cation occupation and grain orientation, are also shown in Fig. 3 to validate the formation of the high-entropy M₃B₄ boride phase for both specimens.

SEM micrographs on polished surfaces shown in Figs. 4(a) and 4(b) illustrate that both specimens are highly dense with porosities of merely 1%–1.5%, which is consistent with the measured nominal relative densities (ignoring the influence of minor secondary phases, since the densities of the M₃B₄ and M₃B₆ phases are similar) of 98.7% for both specimens (Table 1). SEM–EDS elemental maps shown in Figs. 4(c) and 4(d) suggest that most elements distribute homogeneously, albeit some moderate agglomerations of Nb, in both sintered specimens. Furthermore, the quantitative EDS analyses were conducted to measure compositions of the primary phase in the two sintered specimens to be (V_{0.22}Cr_{0.20}Nb_{0.20}Mo_{0.19}Ta_{0.19})₃B₄ and

(V_{0.18}Cr_{0.20}Nb_{0.18}Ta_{0.23}W_{0.21})₃B₄, respectively. The minor differences of 1–3 at% from the nominal equimolar compositions are comparable with the EDS measurement errors. Hence, the nominal compositions are still used in the following discussion.

The combination of XRD, SEM, and EDS demonstrates the formation of high-entropy solid-solution phases of (V_{0.2}Cr_{0.2}Nb_{0.2}Mo_{0.2}Ta_{0.2})₃B₄ and (V_{0.2}Cr_{0.2}Nb_{0.2}Ta_{0.2}W_{0.2})₃B₄ in the Ta₃B₄-prototyped orthorhombic structure. They represent HECs made in yet another new crystal structure and the fourth class of HEBs reported hitherto after high-entropy diborides, hexaborides, and monoborides [8–10,25].

Among all six metal elements, V, Cr, Nb, and Ta have been reported to possess the M₃B₄ orthorhombic phase [31–34]. However, Mo₃B₄ and W₃B₄ have not been reported before, and they are not the thermodynamically stable phases based on the Mo–B and W–B phase diagrams [35]. Yet, this study showed that 20% of Mo₃B₄ and W₃B₄ can be dissolved and stabilized into the high-entropy M₃B₄ boride phases.

The lattice parameters of V₃B₄, Cr₃B₄, Nb₃B₄, and Ta₃B₄ reported in the literature are listed in Table 2, based on which the lattice parameters of four-cation (V_{0.25}Cr_{0.25}Nb_{0.25}Ta_{0.25})₃B₄ can be estimated via the rule-of-mixture (RoM). It can be recognized that both sintered high-entropy M₃B₄ specimens demonstrate

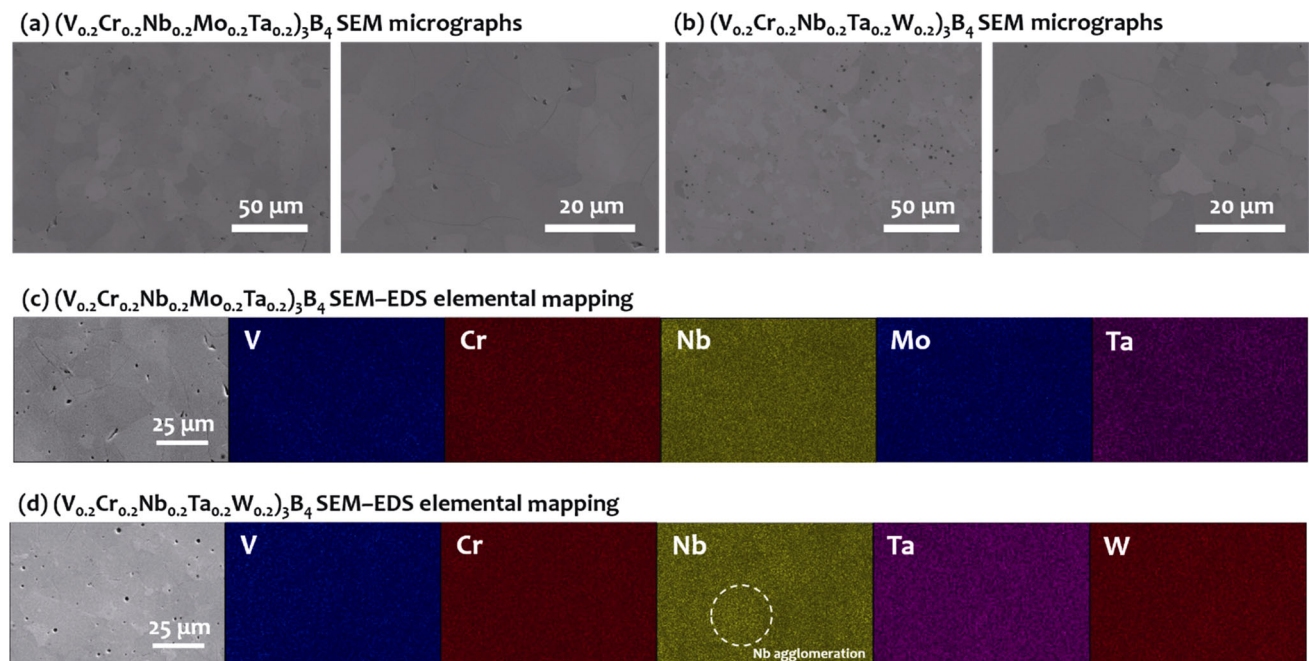


Fig. 4 SEM micrographs of sintered (a) (V_{0.2}Cr_{0.2}Nb_{0.2}Mo_{0.2}Ta_{0.2})₃B₄ and (b) (V_{0.2}Cr_{0.2}Nb_{0.2}Ta_{0.2}W_{0.2})₃B₄ specimens at low and high magnifications, as well as (c, d) the corresponding EDS elemental maps. Most elements distribute uniformly in both specimens, albeit some moderate Nb agglomerations (indicated by the circle in a Nb map, which is not easily distinguishable).

Table 2 Summary of the lattice parameters of four reported Ta_3B_4 -prototyped orthorhombic materials with references. The lattice parameters of four-cation $(V_{0.25}Cr_{0.25}Nb_{0.25}Ta_{0.25})_3B_4$ are calculated based on the rule of mixture

Material	Lattice parameters a, b, c (Å)	Ref.
V_3B_4	3.058, 13.220, 2.981	[31]
Cr_3B_4	3.000, 13.012, 2.952	[32]
Nb_3B_4	3.303, 14.076, 3.143	[33]
Ta_3B_4	3.291, 13.994, 3.133	[34]
$(V_{0.25}Cr_{0.25}Nb_{0.25}Ta_{0.25})_3B_4$	3.163, 13.576, 3.052	—

very small discrepancies ($< 1\%$) in lattice parameters with $(V_{0.25}Cr_{0.25}Nb_{0.25}Ta_{0.25})_3B_4$; a larger lattice parameter b for $(V_{0.2}Cr_{0.2}Nb_{0.2}Mo_{0.2}Ta_{0.2})_3B_4$ over $(V_{0.2}Cr_{0.2}Nb_{0.2}Ta_{0.2}W_{0.2})_3B_4$ is due to the different addition of Mo and W.

The formation of minor secondary M_5B_6 phases may be attributed to insufficient boron (or slight boron loss during the processing). In a HEBM–SPS synthesis route, the addition of extra boron beyond the stoichiometric amount is necessary to remove native oxides and offset any boron loss [22]. However, this practice of adding extra boron, as well as the existence of native oxides in commercial precursors, leads to difficulties in controlling the exact stoichiometry [26]. For the M_3B_4 phases, even 1 at% deficient boron in the final specimen can induce as much as ~ 10 mol% of the M_5B_6 secondary phase. After extensive optimization, a metal-to-boron atomic ratio $\approx 3:4.16$ was adopted to fabricate high-entropy M_3B_4 specimens with no detectable oxide phase and high relative density ($\sim 98.7\%$).

XRD shows that the amount of the secondary phases should be minor (Fig. 3). To estimate the actual

secondary phase fractions in the sintered specimens, SEM micrographs and EBSD maps on multiple areas at different locations have been analyzed and combined. First, digital image processing of a large number of SEM micrographs was used to accurately measure the porosities to be $\sim 1.3\%$ for $(V_{0.2}Cr_{0.2}Nb_{0.2}Mo_{0.2}Ta_{0.2})_3B_4$ and $\sim 1.5\%$ for $(V_{0.2}Cr_{0.2}Nb_{0.2}Ta_{0.2}W_{0.2})_3B_4$, respectively. Second, the (black) un-indexed areas (corresponding to pores plus secondary phases) in the EBSD maps have been measured to be $\sim 5.3\%$ for $(V_{0.2}Cr_{0.2}Nb_{0.2}Mo_{0.2}Ta_{0.2})_3B_4$ and $\sim 6.7\%$ for $(V_{0.2}Cr_{0.2}Nb_{0.2}Ta_{0.2}W_{0.2})_3B_4$, correspondingly. Thus, the volume fractions of the secondary phases in the sintered specimens are determined to be ~ 4.0 vol% for $(V_{0.2}Cr_{0.2}Nb_{0.2}Mo_{0.2}Ta_{0.2})_3B_4$ and ~ 5.2 vol% for $(V_{0.2}Cr_{0.2}Nb_{0.2}Ta_{0.2}W_{0.2})_3B_4$, respectively. The data are summarized in Table 1.

EBSD analyses were also applied to measure the grain size, determine the crystal orientation, and examine the texture. Carried out on a well-polished specimen surface perpendicular to the direction of compressing pressure and current during SPS, EBSD normal direction inverse pole figure orientation maps are shown in Fig. 5. The measured grain size distributions are shown in the insets in Fig. 5, suggesting similar grain size distributions. The means \pm one standard deviations were measured to be $12.2 \pm 10.1 \mu\text{m}$ for $(V_{0.2}Cr_{0.2}Nb_{0.2}Mo_{0.2}Ta_{0.2})_3B_4$ and $12.1 \pm 10.3 \mu\text{m}$ for $(V_{0.2}Cr_{0.2}Nb_{0.2}Ta_{0.2}W_{0.2})_3B_4$, respectively. It is worth noting that both specimens contain some clustered regions of small-size grains, a microstructure feature commonly observed in reactive-SPS-synthesized borides [24,36,37]. While the XRD patterns (Fig. 3) suggest the existence of some texture, especially in $(V_{0.2}Cr_{0.2}Nb_{0.2}Mo_{0.2}Ta_{0.2})_3B_4$, where (150) peak was found to be significantly higher in relative intensity

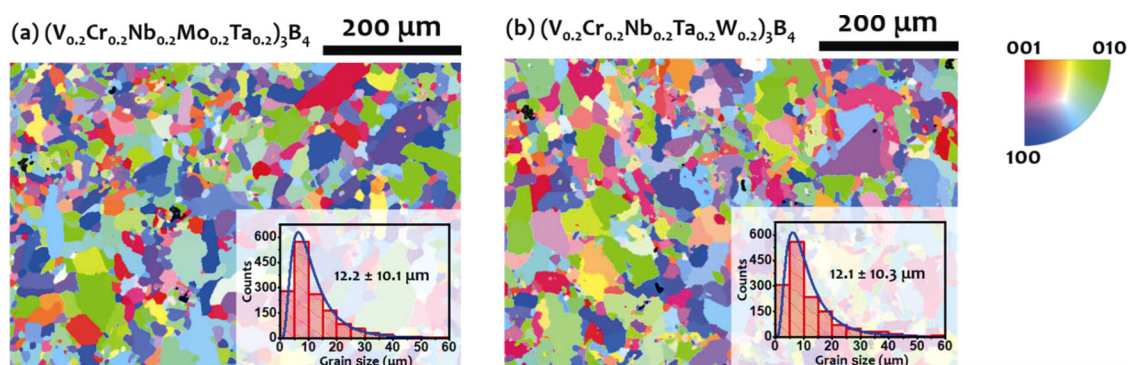


Fig. 5 EBSD normal direction inverse pole figure orientation maps on the plane perpendicular to the pressing and current direction in SPS for (a) $(V_{0.2}Cr_{0.2}Nb_{0.2}Mo_{0.2}Ta_{0.2})_3B_4$ and (b) $(V_{0.2}Cr_{0.2}Nb_{0.2}Ta_{0.2}W_{0.2})_3B_4$. The black domains in the maps are from either pores or secondary phases that cannot be indexed to the high-entropy M_3B_4 phase. The insets show grain size distributions.

than that in the calculated XRD pattern, EBSD maps did not reveal significant texture.

Vickers microhardness values were measured at the standard 9.8 N indentation load to be 18.6 ± 1.2 GPa for $(V_{0.2}Cr_{0.2}Nb_{0.2}Mo_{0.2}Ta_{0.2})_3B_4$ and 19.8 ± 0.9 GPa for $(V_{0.2}Cr_{0.2}Nb_{0.2}Ta_{0.2}W_{0.2})_3B_4$, respectively. These high-entropy M_3B_4 borides are lower in hardness than their high-entropy monoboride counterparts (24.3 and 25.5 GPa, respectively, at 9.8 N for the same cation combinations) fabricated via the similar route [9]. Considering that Cr_3B_4 (14.71 GPa at 0.98 N), Nb_3B_4 (22.46 GPa at 0.29 N), and Ta_3B_4 (32.85 GPa at 0.49 N) are all reported to have hardness values comparable to, or even slightly higher than, their monoboride counterparts (CrB: 12.75 GPa at 0.98 N, NbB: 21.53 GPa at 0.49 N, and TaB: 30.69 GPa at 0.49 N), the relatively low hardness values in the high-entropy M_3B_4 borides, in comparison with high-entropy monoborides, are somewhat unexpected. Note that these hardness data of binary M_3B_4 and MB materials were found in an earlier handbook [38], which were adopted in a recent review [26]. Nonetheless, the hardness values of high-entropy M_3B_4 borides are still comparable to those of some high-entropy diborides [20,39,40].

4 Conclusions

In summary, this study demonstrates the first successful synthesis of Ta_3B_4 -prototyped orthorhombic high-entropy M_3B_4 borides via *in-situ* reactive SPS from elemental boron and metals precursors. The two specimens of $(V_{0.2}Cr_{0.2}Nb_{0.2}Mo_{0.2}Ta_{0.2})_3B_4$ and $(V_{0.2}Cr_{0.2}Nb_{0.2}Ta_{0.2}W_{0.2})_3B_4$ with 4%–5% secondary phases (both of ~ 12 μm averaged grain sizes) have been synthesized in the bulk form with high relative densities ($\sim 98.7\%$) and virtually no detectable oxide impurities. Their Vickers microhardness values at 9.8 N indentation load were measured to be 18.6 and 19.9 GPa, respectively, which are lower than high-entropy monoborides but comparable to high-entropy diborides.

Acknowledgements

This work is partially supported by an office of Naval Research MURI Program (Grant No. N00014-15-1-2863). Qizhang YAN and Jian LUO also acknowledge partial

support from the Air Force Office of Scientific Research (Grant No. FA9550-19-1-01327) for the microscopy work.

References

- [1] Yeh JW, Lin SJ, Chin TS, *et al.* Formation of simple crystal structures in Cu–Co–Ni–Cr–Al–Fe–Ti–V alloys with multiprincipal metallic elements. *Metall Mat Trans A* 2004, **35**: 2533–2536.
- [2] Cantor B, Chang ITH, Knight P, *et al.* Microstructural development in equiatomic multicomponent alloys. *Mater Sci Eng: A* 2004, **375–377**: 213–218.
- [3] Miracle DB, Senkov ON. A critical review of high entropy alloys and related concepts. *Acta Mater* 2017, **122**: 448–511.
- [4] Jiang SC, Hu T, Gild J, *et al.* A new class of high-entropy perovskite oxides. *Scripta Mater* 2018, **142**: 116–120.
- [5] Gild J, Samiee M, Braun JL, *et al.* High-entropy fluorite oxides. *J Eur Ceram Soc* 2018, **38**: 3578–3584.
- [6] Wright AJ, Wang QY, Ko ST, *et al.* Size disorder as a descriptor for predicting reduced thermal conductivity in medium- and high-entropy pyrochlore oxides. *Scripta Mater* 2020, **181**: 76–81.
- [7] Rost CM, Sachet E, Borman T, *et al.* Entropy-stabilized oxides. *Nat Commun* 2015, **6**: 8485.
- [8] Gild J, Zhang YY, Harrington T, *et al.* High-entropy metal diborides: A new class of high-entropy materials and a new type of ultrahigh temperature ceramics. *Sci Rep* 2016, **6**: 37946.
- [9] Qin MD, Yan QZ, Wang HR, *et al.* High-entropy monoborides: Towards superhard materials. *Scripta Mater* 2020, **189**: 101–105.
- [10] Zhao PB, Zhu JP, Zhang YL, *et al.* A novel high-entropy monoboride $(Mo_{0.2}Ta_{0.2}Ni_{0.2}Cr_{0.2}W_{0.2})B$ with superhardness and low thermal conductivity. *Ceram Int* 2020, **46**: 26626–26631.
- [11] Sarker P, Harrington T, Toher C, *et al.* High-entropy high-hardness metal carbides discovered by entropy descriptors. *Nat Commun* 2018, **9**: 4980.
- [12] Harrington TJ, Gild J, Sarker P, *et al.* Phase stability and mechanical properties of novel high entropy transition metal carbides. *Acta Mater* 2019, **166**: 271–280.
- [13] Yan XL, Constantin L, Lu YF, *et al.* $(Hf_{0.2}Zr_{0.2}Ta_{0.2}Nb_{0.2}Ti_{0.2})C$ high-entropy ceramics with low thermal conductivity. *J Am Ceram Soc* 2018, **101**: 4486–4491.
- [14] Gild J, Braun J, Kaufmann K, *et al.* A high-entropy silicide: $(Mo_{0.2}Nb_{0.2}Ta_{0.2}Ti_{0.2}W_{0.2})Si_2$. *J Materiomics* 2019, **5**: 337–343.
- [15] Qin Y, Liu JX, Li F, *et al.* A high entropy silicide by reactive spark plasma sintering. *J Adv Ceram* 2019, **8**: 148–152.
- [16] Chen XQ, Wu YQ. High-entropy transparent fluoride laser ceramics. *J Am Ceram Soc* 2020, **103**: 750–756.
- [17] Wright AJ, Wang QY, Huang CY, *et al.* From high-entropy

- ceramics to compositionally-complex ceramics: A case study of fluorite oxides. *J Eur Ceram Soc* 2020, **40**: 2120–2129.
- [18] Wright AJ, Luo J. A step forward from high-entropy ceramics to compositionally complex ceramics: A new perspective. *J Mater Sci* 2020, **55**: 9812–9827.
- [19] Zhang Y, Jiang ZB, Sun SK, *et al.* Microstructure and mechanical properties of high-entropy borides derived from boro/carbothermal reduction. *J Eur Ceram Soc* 2019, **39**: 3920–3924.
- [20] Gu JF, Zou J, Sun SK, *et al.* Dense and pure high-entropy metal diboride ceramics sintered from self-synthesized powders via boro/carbothermal reduction approach. *Sci China Mater* 2019, **62**: 1898–1909.
- [21] Gild J, Wright A, Quiambao-Tomko K, *et al.* Thermal conductivity and hardness of three single-phase high-entropy metal diborides fabricated by borocarbothermal reduction and spark plasma sintering. *Ceram Int* 2020, **46**: 6906–6913.
- [22] Tallarita G, Licheri R, Garroni S, *et al.* Novel processing route for the fabrication of bulk high-entropy metal diborides. *Scripta Mater* 2019, **158**: 100–104.
- [23] Tallarita G, Licheri R, Garroni S, *et al.* High-entropy transition metal diborides by reactive and non-reactive spark plasma sintering: A comparative investigation. *J Eur Ceram Soc* 2020, **40**: 942–952.
- [24] Qin MD, Gild J, Wang HR, *et al.* Dissolving and stabilizing soft WB_2 and MoB_2 phases into high-entropy borides via boron-metals reactive sintering to attain higher hardness. *J Eur Ceram Soc* 2020, **40**: 4348–4353.
- [25] Chen H, Zhao ZF, Xiang HM, *et al.* Effect of reaction routes on the porosity and permeability of porous high entropy $(Y_{0.2}Yb_{0.2}Sm_{0.2}Nd_{0.2}Eu_{0.2})B_6$ for transpiration cooling. *J Mater Sci Technol* 2020, **38**: 80–85.
- [26] Akopov G, Yeung MT, Kaner RB. Rediscovering the crystal chemistry of borides. *Adv Mater* 2017, **29**: 1604506.
- [27] Rudy E, Windisch S. *Ternary Phase Equilibria in Transition Metal–Boron–Carbon–Silicon Systems, Part I. Related Binary Systems. Volume X. System V–B, Nb–B, and Ta–B.* Air Force Materials Laboratory, Wright-Patterson Air Force Base, OH, 1966.
- [28] Yao TK, Wang YC, Li H, *et al.* A universal trend of structural, mechanical and electronic properties in transition metal (M=V, Nb, and Ta) borides: First-principle calculations. *Comput Mater Sci* 2012, **65**: 302–308.
- [29] Bolmgren H, Lundström T, Tergenius LE, *et al.* The crystal structure of Ta_3B_6 . *J Less Common Met* 1990, **161**: 341–345.
- [30] Spear KE, Liao PK, Smith JF. The B–V (boron–vanadium) system. *J Phase Equilibria* 1987, **8**: 447–454.
- [31] Spear KE, Gilles PW. Phase and structure relationships in the vanadium-boron system. *High Temp Sci* 1969, **1**: 86–97.
- [32] Okada S, Atoda T, Higashi I. Structural investigation of Cr_2B_3 , Cr_3B_4 , and CrB by single-crystal diffractometry. *J Solid State Chem* 1987, **68**: 61–67.
- [33] Okada S, Hamano K, Lundström T, *et al.* Crystal growth of the new compound Nb_2B_3 , and the borides NbB, Nb_5B_6 , Nb_3B_4 , and NbB_2 , using the copper-flux method. *AIP Conf Proc* 1991, **231**: 456–459.
- [34] Okada S, Kudou K, Higashi I, *et al.* Single crystals of TaB, Ta_3B_6 , Ta_3B_4 and TaB_2 , as obtained from high-temperature metal solutions, and their properties. *J Cryst Growth* 1993, **128**: 1120–1124.
- [35] Rudy E, Windisch S. *Ternary Phase Equilibria in Transition Metal–Boron–Carbon–Silicon Systems. Part I. Related Binary Systems. Volume III. Systems Mo–B and W–B.* Air Force Materials Laboratory, Wright-Patterson Air Force Base, OH, 1966.
- [36] Schmidt J, Boehling M, Burkhardt U, *et al.* Preparation of titanium diboride TiB_2 by spark plasma sintering at slow heating rate. *Sci Technol Adv Mater* 2007, **8**: 376–382.
- [37] Ran SL, Zhang L, van der Biest O, *et al.* Pulsed electric current, *in situ* synthesis and sintering of textured TiB_2 ceramics. *J Eur Ceram Soc* 2010, **30**: 1043–1047.
- [38] Ivankov AA. *Handbook of Hardness Data.* Kiev: Naukova Dumka, 1968.
- [39] Qin MD, Gild J, Hu CZ, *et al.* Dual-phase high-entropy ultra-high temperature ceramics. *J Eur Ceram Soc* 2020, **40**: 5037–5050.
- [40] Liu JX, Shen XQ, Wu Y, *et al.* Mechanical properties of hot-pressed high-entropy diboride-based ceramics. *J Adv Ceram* 2020, **9**: 503–510.

Open Access This article is licensed under a Creative Commons Attribution 4.0 International License, which permits use, sharing, adaptation, distribution and reproduction in any medium or format, as long as you give appropriate credit to the original author(s) and the source, provide a link to the Creative Commons licence, and indicate if changes were made.

The images or other third party material in this article are included in the article's Creative Commons licence, unless indicated otherwise in a credit line to the material. If material is not included in the article's Creative Commons licence and your intended use is not permitted by statutory regulation or exceeds the permitted use, you will need to obtain permission directly from the copyright holder.

To view a copy of this licence, visit <http://creativecommons.org/licenses/by/4.0/>.